

Article

Corrosion Behavior and Biological Activity of Micro Arc Oxidation Coatings with Berberine on a Pure Magnesium Surface

Liting Mu ^{1,2}, Zhen Ma ¹, Jingyan Wang ¹, Shidan Yuan ¹ and Muqin Li ^{1,*}

¹ School of Materials Science and Engineering, Jiamusi University, Jiamusi 154007, China; muliting@163.com (L.M.); mz252930179@163.com (Z.M.); jmsdxclwjy@163.com (J.W.); jmsdxysd@163.com (S.Y.)

² School of Pharmacy, Jiamusi University, Jiamusi 154007, China

* Correspondence: limuqin@jmsu.edu.cn; Tel.: +86-454-8618-702

Received: 1 August 2020; Accepted: 22 August 2020; Published: 28 August 2020



Abstract: Bone tissue repair materials can cause problems such as inflammation around the implant, slow bone regeneration, and poor repair quality. In order to solve these problems, a coating was prepared by ultrasonic micro-arc oxidation and self-assembly technology on a pure magnesium substrate. We studied the effect of berberine on the performance of the ultrasonic micro-arc oxidation/polylactic acid and glycolic acid copolymer/berberine (UMAO/PLGA/BR) coating. The chemical and morphological character of the coating was analyzed using scanning electron microscopy, X-ray diffraction, and X-ray photoelectron spectroscopy. The corrosion properties were studied by potentiodynamic polarization and electrochemical impedance spectroscopy in a simulated body fluid. The cumulative release of drugs was tested by high-performance liquid chromatography. The results indicate that different amounts of BR can seal the corrosion channel to different extents. These coatings have a self-corrosion current density (I_{corr}) at least one order of magnitude lower than the UMAO coatings. When the BR content is 3.0 g/L, the self-corrosion current density of the UMAO/PLGA/BR coatings is the lowest (3.14×10^{-8} A/cm²) and the corrosion resistance is improved. UMAO/PLGA/BR coatings have excellent biological activity, which can effectively solve the clinical problem of rapid degradation of pure magnesium and easy infection.

Keywords: pure magnesium; ultrasonic micro-arc oxidation; berberine; corrosion resistance

1. Introduction

Traumatic bone repair materials have become a research hotspot in the field of orthopedics. They are mainly derived from autologous and allogeneic bone grafts [1]. The source of autologous bone grafting materials is limited, complications are prone to occur after surgery, and the success rate is low. Allogeneic bone graft materials are expensive and prone to rejection. The degradation of allogeneic bone is slow, resulting in a smaller volume of new bone. In order to solve the above problems, material researchers are trying to find suitable human bone repair materials. With the development of biodegradable materials, metal bone repair biomaterials are undergoing a revolution. The properties of metal biomaterials have changed from being biologically inert to having biological activity and multiple biological functions [2,3]. Magnesium and magnesium alloys are characterized by good osteoinductivity, spontaneous degradability, and excellent biological safety. Their mechanical properties are similar to those of human cortical bone, and the biological properties of the graft are similar to those of natural bone, which has attracted a great amount of attention in the bone repair materials field [4,5]. The degradable properties of magnesium will eliminate the need for a second surgery to remove the implant. Thus, magnesium and magnesium alloy bone repair materials would

not only further reduce the pain and burden for patients, but also increase the application of these advanced materials [6]. However, a series of biological problems have been discovered during the clinical application of pure magnesium, such as osteolysis around the implant, easy loosening of the implant, rapid degradation, and hemolytic infection, which limit the application of pure medical magnesium and magnesium alloys [7–9].

Therefore, researchers should study composite coatings with antibacterial, anti-inflammatory, and bone growth promotion effects, and then adjust and control the degradation rate and biological characteristics of pure medical magnesium to solve the fundamental problem of magnesium implants and make magnesium more suitable as an implant material [10]. In recent years, ultrasonic micro-arc oxidation (UMAO) has been shown to be an effective surface modification technology that can effectively reduce the degradation rate of materials [11,12]. UMAO can effectively improve the corrosion resistance of magnesium alloys. However, the micropores and microcracks of the UMAO surface may cause undesirable rapid and unexpected degradation of magnesium and its alloys [13]. Therefore, scholars have tried to compound other surface modification technologies on the UMAO surface [14–16]. Li [17] reported using KH550 as a silane coupling agent to modify the surface of the ultrasonic micro-arc oxidation coating on pure magnesium. The organic film of the Si–O–Mg bond formed on the surface helps to reduce the pores in the UMAO coating and improve its corrosion resistance. In order to further improve the bone growth around the implant, as well as the antibacterial and anti-inflammatory effects, Peng [18] prepared a phytic acid puerarin solution on the UMAO coating by dip coating. The composite coating has better corrosion resistance than UMAO. It also accelerates the mineralization of apatite and improves the biological activity. Wang [19] prepared an UMAO/chitosan/citrin coating on a pure Mg substrate. They found that the Chinese herbal extract coating enhanced the corrosion resistance and biological activity of pure Mg, and also enhanced the adhesion and proliferation of osteoblasts. However, the coating drug released quickly and the concentration was low. Furthermore, its ability to promote bone growth, as well as its antibacterial and anti-inflammatory effects, did not reach the expected effect.

The most difficult problem with these coatings in bone injury is the low drug concentration at the lesion site. If the drug concentration around the local implant is maintained in a reasonable range, it will be slowly released around the implantation area at a certain rate within a certain period of time to achieve the purpose of the treatment. At present, long-acting sustained-release drug-loaded artificial bone is considered feasible [20,21]. The preparation of drug-loaded artificial bone usually includes methods such as the vacuum adsorption freeze-drying method and the compression molding method. The above methods can achieve the effect of sustained drug release. However, studies have found that the release of drugs is too fast or the drug-carrying materials cannot be degraded or they degrade very slowly, which limits the application [22–24]. Polylactic acid glycolic acid copolymer (PLGA) is a degradable functional polymer organic compound, usually used as a carrier for drug release [25]. PLGA is widely used in the fields of pharmaceutical and medical engineering materials, mainly because it is biocompatible, non-toxic, shows controllable degradation, and produces harmless metabolites in the body. It also has excellent coating-forming properties. At the same time, PLGA as a biomedical material has been certified by the U.S. Food and Drug Administration. Sevostyanov [26] studied the coating of PLGA-containing triple anti-tuberculosis patients' bones, which can stably and slowly release drugs and maintain the local drug concentration at a high level in the lesion. Qian [27] found that the degradation of PLGA in the human body is acidic, and magnesium is degraded to alkaline. After degradation, the environment is neutralized to a certain extent. Wu [28] prepared magnesium-enhanced PLGA copolymer composites by extraction and oil bath methods, and found that the pH of the environment during the degradation process is normal, does not affect bone growth, and can effectively regulate the strength and characteristics of the material according to the location and characteristics of the repaired bone degradation rate.

Until now, PLGA has mostly been used as a carrier for the preparation of slow-release Western medicines. At present, the focus of attention has shifted from synthetic medicine to natural medicine

(Chinese medicine), mainly because traditional Chinese medicine has the characteristics of stable action, low toxicity, and natural materials. Traditional Chinese medicine plays a positive role in promoting the growth of osteoblasts, has antibacterial and anti-inflammatory effects, and is able to regulate the differentiation and biological activity of osteoblasts. Berberine (BR), the main active component of the Chinese medicine *Coptis*, has a variety of biological activities, such as inhibiting inflammation, promoting bone formation, and inhibiting osteoclasts [29,30]. However, few reports have focused on combining PLGA and BR to form a composite sustained-release drug coating to enhance the biological activity and corrosion resistance of magnesium alloys [31].

In this study, by modifying the surface of pure magnesium, we obtain a PLGA/BR multi-element composite functional coating that has antibacterial function, promotes bone growth, and can control the degradation rate, and the structural characteristics, corrosion resistance, and biological activity of the composite coating are systematically evaluated.

2. Materials and Methods

2.1. Materials and Drugs

Mg (Technology Co., Ltd., Yi'an, China) was cut into $10 \times 10 \times 1$ mm sample cubes. The molecular weight of PLGA (polylactic acid/glycolic acid, 50:50) was 90,000 (Daigang Biological Engineering Co., Ltd., Jinan, China), and the berberine content was 99% (China Institute for Food and Drug Control).

2.2. Sample Preparation

Sandpaper was used to polish the samples to a smooth surface; which were then soaked and degreased with ethanol for 30 min; and then cleaned with deionized water, dried, and sealed for later use. The following electrolytes were used in UMAO: $\text{Na}_2\text{SiO}_3 \cdot 9\text{H}_2\text{O}$ (15 g/L), KOH (10 g/L), KF (8 g/L), and $\text{C}_{10}\text{H}_{14}\text{N}_2\text{Na}_2\text{O}_8$ (1 g/L). The working parameters for the UMAO treatment were as follows: first, a pulse width of 50 μs , a pulse frequency of 500 Hz, an auxiliary ultrasonic frequency of 60 kHz, an ultrasonic power of 50 W, a voltage of 300 V, and an oxidation time of 7 min; and second, a regulated voltage of 260 V and an oxidation time of 3 min, cleaned with deionized water and dried in air.

The composite coating was prepared by immersion in 3 mol/L NaOH solution at 60 °C for 1 h, referred to as alkali treatment. Then, 500 mg of PLGA was dissolved in 10 mL of dichloromethane under ultrasound for 30 min. BR-loaded solutions in concentrations of 1.5 g/L, 3.0 g/L, and 6.0 g/L were prepared ultrasonically using the 50 g/L PLGA solution as the solvent for 30 min, giving a self-assembly solution. The sample was immersed in the self-assembly solution for 3 min. Then, the sample was removed from the solution in the vertical direction at a speed of 5 cm/min and dried in air. UMAO/PLGA/BR coatings were marked as 1.5, 3.0, and 6.0 g/L, respectively.

2.3. Coating Characterization

The microstructure and elemental composition of the coatings were characterized by scanning electron microscopy (SEM, JSM-7800JJEOL, Tokyo, Japan) and energy dispersive spectroscopy (EDAX, FALCON60S, Mahwah, NJ, USA). The phases in the coatings were identified by X-ray diffraction (XRD, D8 ADVANCE, BRUKER, Karlsruhe, Germany) with $\text{Cu K}\alpha$ radiation in the 2θ range of 10° to 90° . The contact angle of the coatings was measured by a contact angle meter (JC2000C1, Zhongchen, Shanghai, China). The micro-roughness of the coatings was observed by German Bruker atomic force microscopy (AFM, BRUKER, Karlsruhe, Germany). X-ray photoelectron spectroscopy (XPS, ESCALAB250XI, Thermo Fisher Scientific, Waltham, MA, USA) was used to qualitatively analyze the presence of elements, carbon components, and chemical bonds on the sample surface. The excitation source was $\text{Al K}\alpha$, the test power was 300 W, and C1s (binding energy 284.8 eV) was used before the test to correct the charge displacement of each element in the test. For the XPS peak, software was used to fit the peaks of the high-resolution XPS spectra of the corrected elements.

2.4. Electrochemical Test

The electrochemical impedance spectroscopy (EIS) and the Tafel curve measurements of the coating were performed by a VersaSTAT 3 electrochemical workstation in the simulated body fluid (SBF) solution at 37 °C to evaluate the corrosion behavior of the coating. SBF [32] composition is shown in Table 1. All reagents comply with American Chemical Society standards (ACS). The frequency range of EIS measurements was 10^{-1} – 10^4 Hz. ZsimpWin software was used to perform equivalent circuit fitting on the impedance results.

Table 1. Chemical composition and reagents grade (ACS, American Chemical Society standards) and purity used for preparation of simulated body fluid (SBF).

No.	Chemical Formula	Amount	Reagent Grade	Purity	Manufacturer
1	NaCl	8.035 g/L	ACS reagent	≥99.90%	
2	NaHCO ₃	0.355 g/L	Bio Reagent	≥99.50%	
3	KCl	0.225 g/L	ACS reagent	≥99.50%	
4	K ₂ HPO ₄ ·3H ₂ O	0.231 g/L	ACS reagent	≥99.90%	Comeo Co., Ltd., Tianjin, China
5	MgCl ₂ ·6H ₂ O	0.311 g/L	ACS reagent	≥98.00%	
6	1.0M-HCl	39 mL	ACS reagent	≥37.00%	
7	CaCl ₂	0.292 g/L	ACS reagent	≥99.90%	
8	Na ₂ SO ₄	0.072 g/L	ACS reagent	≥99.90%	
9	(CH ₂ OH) ₃ CNH ₂	6.118 g/L	Standard & Buffer	≥99.90%	

2.5. Immersion Tests

The temperature of the experiment was maintained at 37.0 ± 0.5 °C using a constant temperature water bath and soaked for 3, 7, and 14 days. The degradation and corrosion resistance of the composite bio-coating was identified by SEM. The morphology and composition of the sample before and after immersion were analyzed and studied.

2.6. Slow-Release Drug Measurement

A high-performance liquid chromatography (HPLC) method was established for the qualitative analysis of berberine standard products. The chromatographic conditions were selected as follows: column: Hypersil GOLD C₁₈ (100 × 2.1 mm, 1.9 μm); mobile phase: 0.1% formic acid–acetonitrile/0.1% formic acid water (A/B = 30:70); flow rate: 0.3 mL/min, temperature: 40 °C; injection volume: 10 μL; detection wavelength: 345 nm. A constant temperature method was used for the in vitro drug release test. The samples were sealed and placed in an eppendorf (EP) tube, added to a simulated body fluid with a pH of 7.4, and placed in a 37 °C incubator to simulate the growth environment. Samples were taken after 1, 3, 5, 7, 9, 11, 13, 15, 17, 19, 21, 23, 25, 27, 29, and 31 d. Then, 40 μL of the sample was added to 360 μL methanol, and the same amount of simulated body fluid was added to the EP tube. The sample was injected into the HPLC, the peak area was recorded at 345 nm, and the cumulative release of BR was calculated using the peak area. The time was the abscissa and the cumulative release rate was the ordinate to draw the release curve, and analyze the results.

3. Results and Discussion

3.1. SEM Analysis

The surface morphologies of the various coatings were characterized by SEM, as shown in Figure 1. The surface of the UMAO coating had a porous honeycomb structure typical of the micro-arc oxidation process [33,34], as shown in Figure 1a. The porous structure of the coating surface became a channel for body fluids to etch the substrate, which corroded the pure Mg substrate. The surface of the UMAO/PLGA/BR coatings was covered by PLGA/BR coating (Figure 1b–d). When the BR content was

1.5 g/L, the morphology of the micro-arc oxidation began to be obscured. When the content of BR was 3.0 g/L and 6.0 g/L, the surface morphology of the coating changed significantly. Most of the micro-arc oxidation morphology was filled by PLGA/BR, so the pore size and number were reduced, with better compactness. As the amount of the drug increased, the morphology of the micro-arc oxidation was more completely covered. As PLGA was acidic after degradation, the coating had some holes, and the degraded magnesium could be neutralized with PLGA degradation that was produced to avoid a local pH that was too low or too high [35].

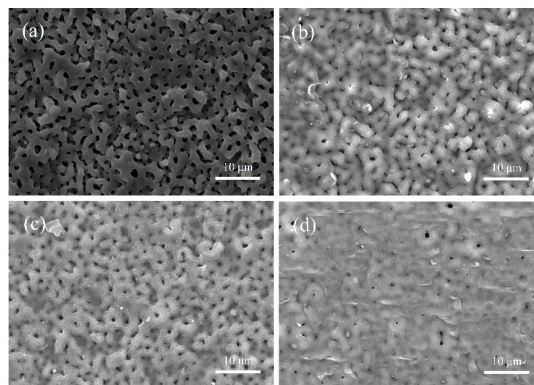


Figure 1. Scanning electron microscopy (SEM) cross-sectional morphologies of various coatings: (a) ultrasonic micro-arc oxidation (UMAO); (b) UMAO/poly(lactic acid and glycolic acid copolymer (PLGA)/berberine (BR)1.5; (c) UMAO/PLGA/BR3.0; (d) UMAO/PLGA/BR6.0.

The cross-sectional morphologies of the coatings with different amounts of BR were characterized by SEM, as shown in Figure 2. Obvious through holes were seen in the UMAO coating section, and the coating thickness was 4.8 µm (Figure 2a). UMAO/PLGA/BR coatings had obvious double-layer superimposed structures, and the interface between the UMAO layer and the PLGA/BR layer was very clear. When the concentration of BR was 1.5 g/L, UMAO through holes were reduced, and the coating thickness was 5.4 µm (Figure 2b). At 3.0 g/L of BR, the UMAO through holes were significantly reduced, and the coating thickness was 7.7 µm (Figure 2c). Compared with the research of Peng [18], the coating thickness increases and the coating becomes denser. At 6.0 g/L of BR, the coating was dense and the coating thickness was 6.0 µm (Figure 2d). Comparative analysis of the cross-sectional morphology of the coating showed that, with the increase of the amount of BR, the thickness of the coating first increased and then decreased, but the overall coating thicknesses increased and the corrosion channels were better filled. When the BR drug content reached 3.0 and 6.0 g/L, the cross sections of the coatings were denser, and the bonding effect between the coatings was better.

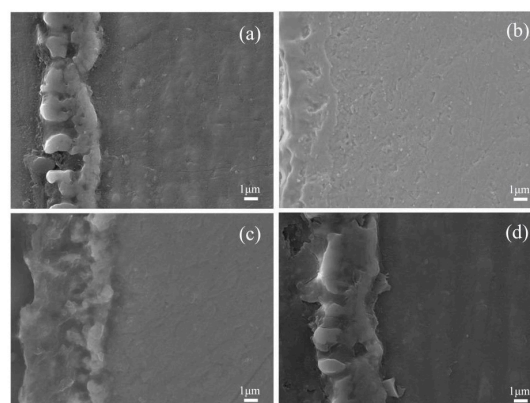


Figure 2. SEM cross-sectional morphologies of various coatings: (a) UMAO; (b) UMAO/PLGA/BR1.5; (c) UMAO/PLGA/BR3.0; (d) UMAO/PLGA/BR6.0.

3.2. Phase Analysis of the Coatings

All the samples were investigated from the phase structural point of view. The phase structures of the various coatings were characterized by XRD, as shown in Figure 3. Contrasted with international centre diffraction data (ICDD). The UMAO coating mainly consisted of MgO (ICDD file no. 65-0476) and Mg₂SiO₄ (ICDD file no. 83-1807) phase [36,37]. MgO and Mg₂SiO₄ phase were detected UMAO/PLGA/BR coatings. In addition, owing to the thin film, the Mg phase was detected in various coatings (ICDD file no. 35-0821).

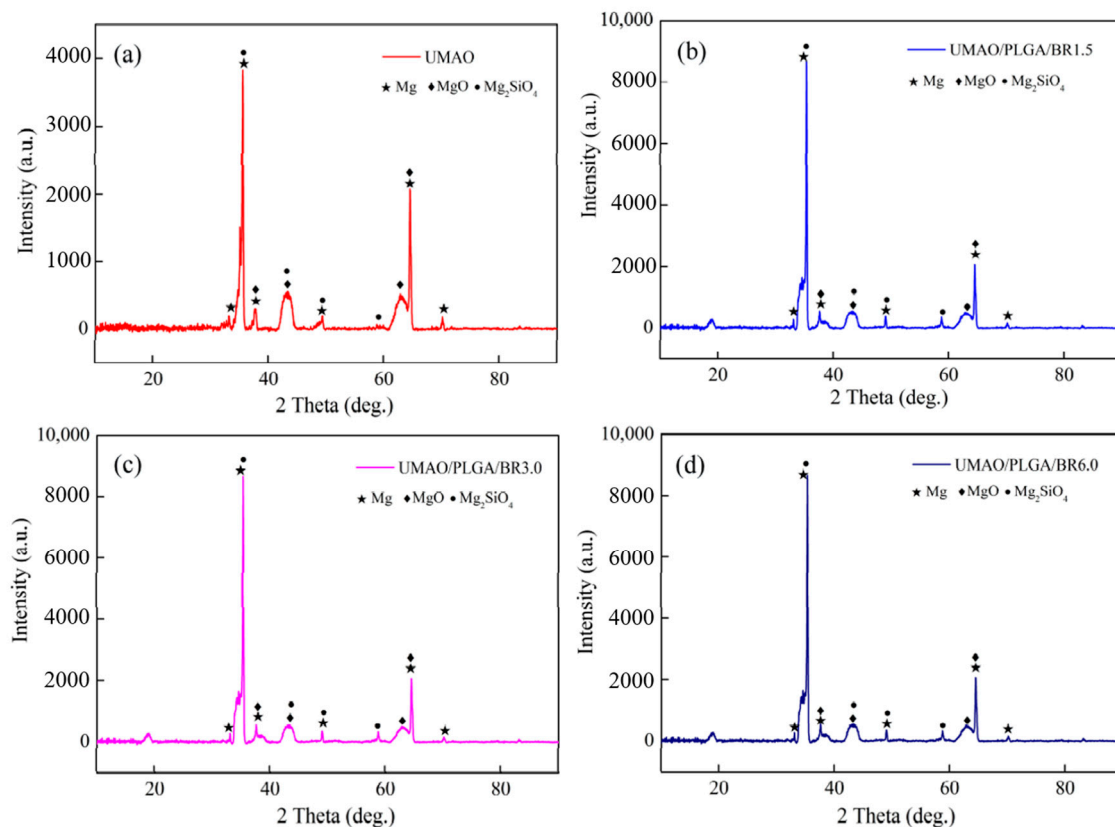


Figure 3. X-ray diffraction (XRD) patterns of coatings with various BR contents: (a) UMAO; (b) UMAO/PLGA/BR1.5; (c) UMAO/PLGA/BR3.0; (d) UMAO/PLGA/BR6.0.

3.3. Contact Angle Analysis

The wettability of the various coatings was determined by the static water contact angle, as shown in Figure 4. The five contact angles measured by various coatings are shown in Table 2. The water contact angle on the UMAO coating was $20.63 \pm 0.56^\circ$ (Figure 4a). Because the surface of the UMAO coating had higher porosity, the contact angle of the coating was smaller. The water contact angles of the UMAO/PLGA/BR (1.5 g/L), UMAO/PLGA/BR (3.0 g/L), and UMAO/PLGA/BR (6.0 g/L) coatings were $68.12 \pm 0.96^\circ$, $69.73 \pm 0.83^\circ$, and $70.46 \pm 0.89^\circ$, respectively (Figure 4b–d). After UMAO self-assembled BR treatment, the contact angle of the coating increased significantly, restricting the entry of corrosive media and improving the corrosion resistance of the coating [38]. However, the angle was less than 90° , and the hydrophilic coating did not affect cell adhesion.

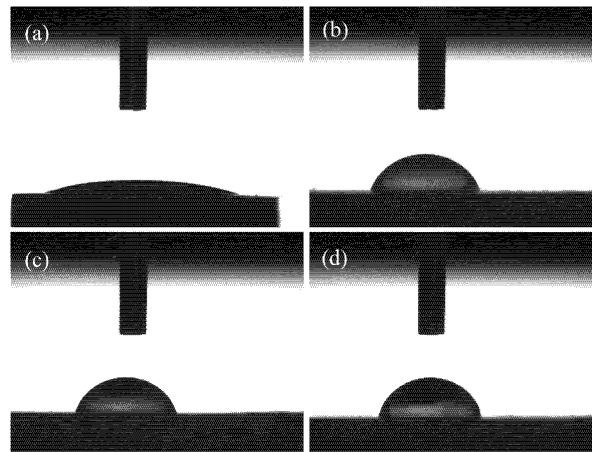


Figure 4. Contact angles of UMAO and coatings with BR on pure magnesium: (a) UMAO; (b) UMAO/PLGA/BR1.5; (c) UMAO/PLGA/BR3.0; (d) UMAO/PLGA/BR6.0.

Table 2. Contact angle of various coatings. UMAO, ultrasonic micro-arc oxidation; BR, berberine.

Sample	UMAO	BR (1.5 g/L)	BR (3.0 g/L)	BR (6.0 g/L)
contact angle 1	20.13°	67.42°	70.23°	71.35°
contact angle 2	20.07°	69.08°	69.53°	69.64°
contact angle 3	20.93°	68.42°	68.90°	71.12°
contact angle 4	21.19°	67.16°	69.43°	70.62°
contact angle 5	20.83°	68.52°	70.56°	69.57°
average value	20.63 ± 0.56°	68.12 ± 0.96°	69.73 ± 0.83°	70.46 ± 0.89°

3.4. Coating Roughness

The micro-roughness of the coatings was observed by German Bruker atomic force microscopy (AFM). The roughnesses of the coatings with different amounts of BR are shown in Figure 5. The BR changed the micro-roughness of the various coatings. The surface of the UMAO membrane was densely populated with raised cells and hills, the size was obviously increased, and the roughness arithmetic (Ra) value was larger (Figure 5a). The surface roughness of BR (1.5 g/L) showed a downward trend, which effectively eliminated the bumps on the surface of the UMAO and reduced the surface roughness of the coating (Figure 5b). With the increase in BR content, the surface roughness value showed an increasing trend. At 3.0 g/L of BR, the bulges and depressions on the film surface increased, and the roughness of the coating became larger (Figure 5c). The surface roughness at 6.0 g/L of BR became smaller. This was because BR further filled the holes in the coating surface and the coating became flat (Figure 5d). It was seen that the amount of BR added greatly affected the Ra value of the UMAO/PLGA/BR coating. The specific roughness values are shown in Table 3.

Table 3. Roughness values of various coatings.

Sample	UMAO	BR (1.5 g/L)	BR (3.0 g/L)	BR (6.0 g/L)
Roughnesses (nm)	246	92.4	190	145

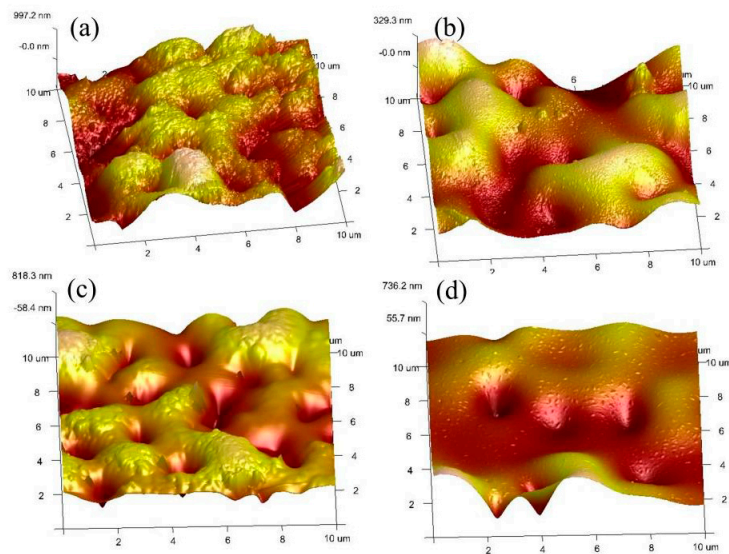


Figure 5. Atomic force microscopy (AFM) images of coatings with various BR contents: (a) UMAO; (b) UMAO/PLGA/BR1.5; (c) UMAO/PLGA/BR3.0; (d) UMAO/PLGA/BR6.0.

3.5. XPS Analysis

XPS measurements were carried out to characterize the composition of the coatings, as shown in Figure 6. Figure 6a illustrates the XPS survey spectra of the different coatings. The chemical composition and element state of the composite coatings were determined. The BR (1.5), BR (3.0), and BR (6.0) coatings all produced spectral peaks of Mg, C, O elements, and this result was consistent with the surface morphology of the coating.

Figure 6b–d illustrate the fine fitting spectra of the O, C, and N elements of the BR (3.0) coating. Using the BR (3.0) coating as an example, the peaks of the UMAO/PLGA/BR coating were analyzed. The fine fitting spectrum of the BR (3.0) coating is shown in Figure 6b–d. According to the further peak analysis of O 1s (shown in Figure 6b), the distinctive peak at 530.8 eV in its fine spectrum is the binding energy of the oxygen element in the Mg–O bond [39]. Figure 6b illustrates the O 1s XPS pattern for the UMAO/PLGA/BR coating, in which the Mg–O bond was present at a binding energy of 530.8 eV and the O element of the –OH was present at a binding energy of 531.4 eV. Figure 6c illustrates the fine spectrum of C 1s. There were two characteristic peaks at 286.3 eV and 284.6 eV in the fine spectrum of C 1s. The characteristic peak at 286.3 eV was attributed to the binding energy of C elements in –C–O– in PLGA. The characteristic peak at 284.6 eV was attributed to the binding energy of the C element in –C–H and –C–C– in PLGA and the binding energy of the C=C functional group C in BR [40,41]. Figure 6d illustrates the fine spectrum of N 1s. The characteristic peaks at 398.6 eV and 399.7 eV were attributed to C–N in BR [42]. It was further seen that, after changing the amount of BR, UMAO/PLGA/BR coating materials were self-assembled on the surface of the pure magnesium substrate.

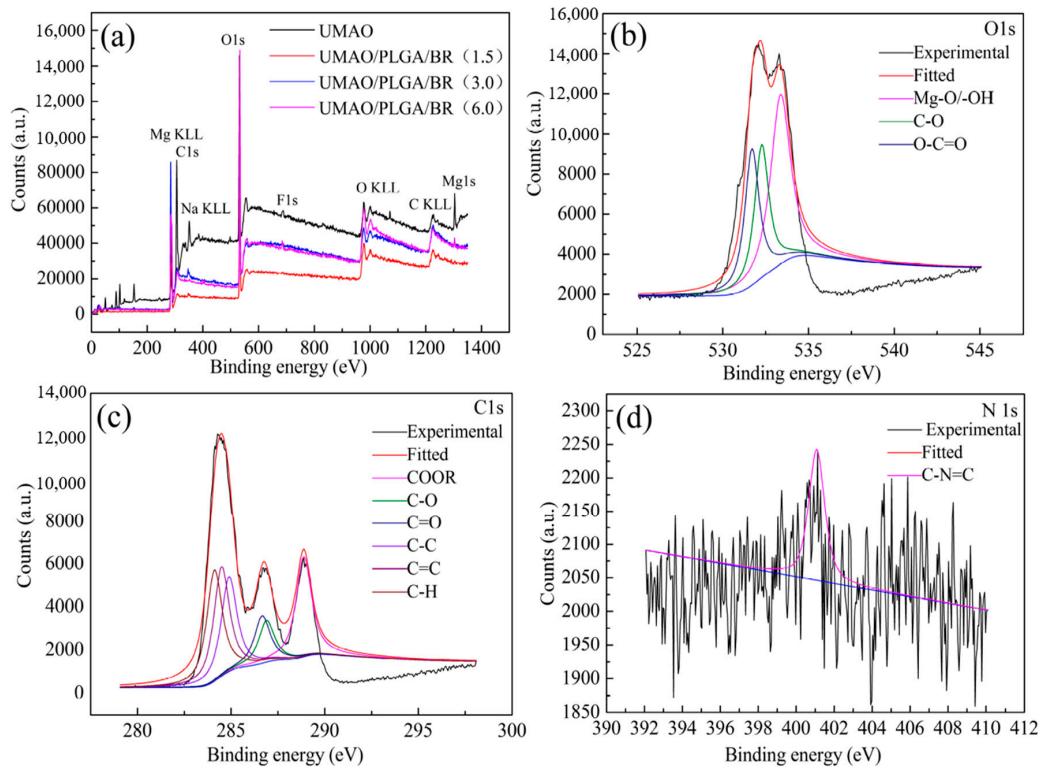


Figure 6. X-ray photoelectron spectroscopy (XPS) spectra of coatings with various BR additions: (a) survey spectrum; (b) O 1s spectra; (c) C 1s spectra; (d) N 1s spectra.

3.6. Corrosion Resistance

The polarization curves of the UMAO, 1.5 g/L, 3.0 g/L, and 6.0 g/L samples are shown in Figure 7. Relevant electrochemical values were obtained by fitting. The corrosion current density (I_{corr}) of the UMAO, UMAO/PLGA/BR (1.5 g/L), UMAO/PLGA/BR (3.0 g/L), and UMAO/PLGA/BR (6.0 g/L) coatings was 2.26×10^{-6} , 3.33×10^{-7} , 3.14×10^{-8} , and 1.26×10^{-7} A/cm², respectively. The more positive corrosion voltage (E_{corr}), smaller corrosion rate (CR) and I_{corr} demonstrate that BR (3.0 g/L) improves the corrosion resistance of Mg by forming the modified structure as described previously [43]. The corresponding fitting parameters are shown in Table 4.

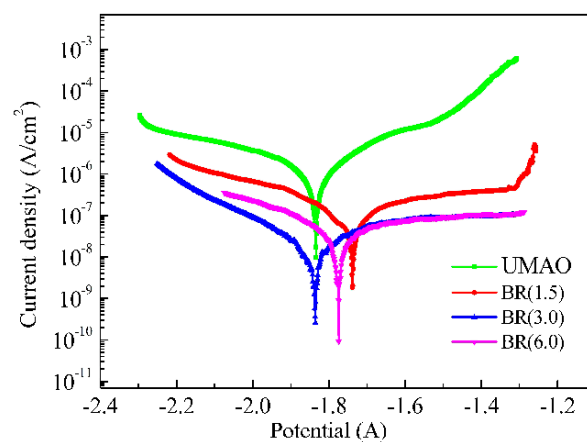


Figure 7. Potentiodynamic polarization curves of various samples.

The I_{corr} of UMAO/PLGA/BR coatings with different BR content was at least one order of magnitude lower than that of UMAO. For the coating prepared by Zhang [44], the corrosion current

of magnesium alloy in simulated body fluid was 2.05×10^{-6} A/cm². This illustrates that coatings with different amounts of BR protected magnesium substrates more effectively than UMAO coatings. In addition, among the drug-loaded coatings, the UMAO/PLGA/BR (3.0 g/L) coating had the lowest I_{corr} value. It is well known that the E_{corr} can describe the thermodynamic property, so the corrosion resistance cannot be evaluated in terms of E_{corr} [45]. It can be concluded that the UMAO/PLGA/BR (3.0 g/L) coating showed a lower corrosion rate and corrosion current density compared with other coatings. It was inferred that the corrosion resistance of the 3.0 g/L coating was the best.

Table 4. Corrosion current densities and corrosion potentials for different coatings in SBF at 37 ± 1 °C. I_{corr}, corrosion current density; E_{corr}, corrosion voltage; CR, corrosion rate.

Sample	UMAO	BR (1.5 g/L)	BR (3.0 g/L)	BR (6.0 g/L)
E _{corr} (V)	-1.834 ± 0.007	-1.741 ± 0.006	-1.872 ± 0.007	-1.769 ± 0.006
I _{corr} (A/cm ²)	$(2.26 \pm 0.02) \times 10^{-6}$	$(3.33 \pm 0.019) \times 10^{-7}$	$(3.14 \pm 0.017) \times 10^{-8}$	$(1.26 \pm 0.023) \times 10^{-7}$
CR (mm/yr)	5.16×10^{-3}	7.60×10^{-4}	7.17×10^{-5}	2.88×10^{-4}

To further analyze the corrosion behavior of the various coatings, EIS measurements were performed in the SBF, as shown in Figure 8. The EIS measurements were analyzed using ZsimpWin software and fitted to the appropriate equivalent circuit. The symbols represent the experimental data, and the solid lines represent the fitted data. Figure 8a shows the Nyquist plots of the samples. The Nyquist plot of the UMAO coating is composed of a capacitive loop. The capacitive loop at the high frequency is attributed to the resistance and capacitance of the electrolyte penetrating through the UMAO layer [46]. The Nyquist plots of the UMAO/PLGA/BR coatings are composed of widened capacitive loops. The capacitive loop is attributed to the resistance and capacitance of the electrolyte penetrating through the PLGA/BR layer at the medium frequency [47]. The radii of the semicircles corresponding to the UMAO/PLGA/BR coating were visibly larger than those of the UMAO coating. These results reveal that the UMAO/PLGA/BR coating has a higher impedance value and higher corrosion resistance.

Figure 8b shows the impedance modulus |Z| of different coatings, which were 4.20×10^4 (UMAO), 5.24×10^5 (BR 1.5 g/L), 1.68×10^6 (BR 3.0 g/L), and 1.41×10^6 (BR 6.0 g/L) Ω·cm². The impedance modulus of the drug-loaded coatings was an order of magnitude higher than that of the UMAO coating. However, after the addition of 6.0 g/L BR, the impedance modulus value of the UMAO/PLGA/BR coating did not continue to increase. Because the solution was a suspension when 6.0 g/L of BR was added, it was not conducive to the formation of self-assembled coatings. As we all know, good corrosion resistance between the coating and the electrolyte corresponds to a higher R value [48,49]. The results showed that, when the amount of BR was 3.0 g/L, the coating had higher resistance and better corrosion resistance.

The Bode plots of the coatings with different amounts of BR are shown in Figure 8c. The shapes were similar. Both coatings have two time constants distributed at a low frequency (10^{-1} – 10^2 Hz) and a high frequency (10^2 – 10^4 Hz). The low-frequency time constant is the response of the UMAO coating, and the high-frequency time constant is the response of the PLGA and PLGA/BR layers [46].

The time constant of the high frequency zone was ascribed to the PLGA/BR layer, and the time constant of the low frequency zone was ascribed to the UMAO layer. The phase angles of BR (1.5), BR (3.0), and BR (6.0) coatings were 65°, 68°, and 62°, respectively. When the amount of BR added reached 3.0 g/L, the phase angle of the coating was the largest and the corrosion resistance was the highest. The Nyquist diagram of the composite coating was consistent with the results of the Bode diagram, indicating that the BR (3.0) coating had good corrosion resistance.

The equivalent circuit used to fit the electrochemical impedance plot of the coatings is shown in Figure 8d. The corresponding fitting parameters are shown in Table 5. In the circuit, R_s is the solution resistance, R₁ is the resistance of the UMAO coating, and R₂ is the resistance of the PLGA/BR coating. CPE₁ (capacitance of coating) and CPE₂ are constant phase angle components of electric double layer capacitors, which represent the capacitive reactance of the UMAO dense layer coating and the

PLGA/BR drug-loaded layer, respectively. In UMAO, R_2 and CPE_2 represent load transfer resistance and interface electric double layer capacitance, respectively. The impedance of the drug-loaded coating was greater than that of the UMAO coating, indicating that the drug-loaded coating could prevent corrosion more effectively [50].

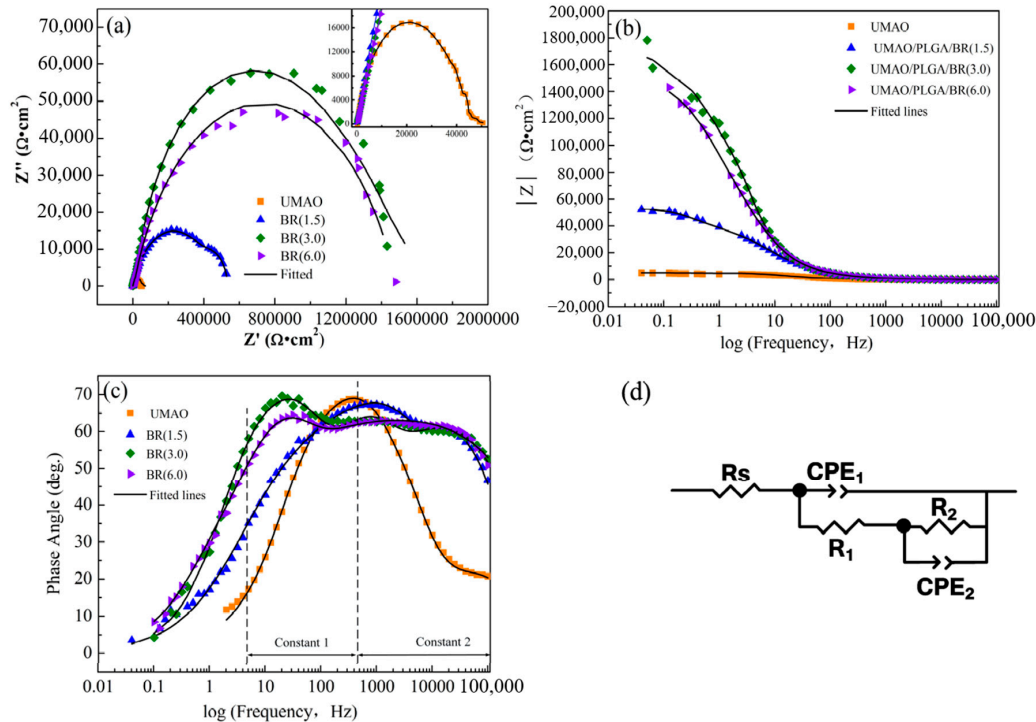


Figure 8. Nyquist, Bode diagrams and equivalent circuits of different coatings: (a) Nyquist; (b) and (c) Bode plots; (d) equivalent circuit (CPE, capacitance of coating).

Table 5. Values of the equivalent circuit parameters for the various coatings extracted from the electrochemical impedance spectroscopy (EIS) plots. CPE, capacitance of coating.

Sample	R_s ($\Omega\cdot\text{cm}^2$)	CPE_1 ($\text{F}\cdot\text{cm}^2$)	R_1 ($\Omega\cdot\text{cm}^2$)	CPE_2 ($\text{F}\cdot\text{cm}^2$)	R_2 ($\Omega\cdot\text{cm}^2$)
UMAO	269.2	4.35×10^{-7}	4.37×10^4	2.59×10^{-5}	1.18×10^4
BR1.5	126.9	1.67×10^{-7}	4.31×10^5	4.16×10^{-6}	1.17×10^5
BR3.0	152.1	1.09×10^{-7}	7.02×10^5	1.06×10^{-8}	1.61×10^6
BR6.0	117.9	1.46×10^{-7}	1.95×10^5	7.49×10^{-9}	1.29×10^6

Therefore, a conclusion can be drawn from the polarization curve and the EIS impedance; that is, the corrosion resistance of the coating was improved by doping BR in the PLGA solution to form a drug-loaded coating. The main reason was that the addition of BR to the PLGA solution was equivalent to a filler, which can fully block the defects, such as pores, of the ceramic layer in the drug-loaded coating and prevent the body fluid from penetrating the Mg matrix too quickly, thereby improving the corrosion resistance.

3.7. Surface Morphology and Phase Composition Analysis in SBF

SEM images of UMAO and UMAO/PLGA/BR (3.0) coatings soaked in SBF solution for 0, 3, 7, and 14 days are shown in Figure 9. Figure 9a₁,b₁ shows the surface morphology of UMAO coating and UMAO/PLGA/BR coating without soaking. Compared with the UMAO coating, after 3 days of soaking, the surface of the coating was gray, and insect-like substances were deposited on the surface of the UMAO film around the pores (Figure 9a₂,b₂). After being immersed for 7 days, cracks appeared on the surface of the coating, and white deposits in the shape of flower clusters were attached to the

cracks. This deposit can effectively fill the cracks and form a new composite surface to prevent the corrosive medium from passing through the pores or cracks (Figure 9a₃,b₃), which was also reported in other studies [51,52]. After 14 days of soaking, the cracks deepened, the number increased, and the white deposits increased. The surface of the coating material became rough, and its surface area increased to provide an interface for ion adsorption (Figure 9a₄,b₄). Because of the extension in the immersion time, Ca and P elements were enriched and nucleated on the surface, and the mass increased with time. At the same time, Mg ions gradually degraded from the surface and were replaced by Ca ions, which adsorb more CO₃²⁻ and PO₄³⁻ on the surface of the coating material; when the solubility product of forming bone-like apatite was reached, a new phase was formed on the surface [53,54], so the BR coating had excellent biological activity.

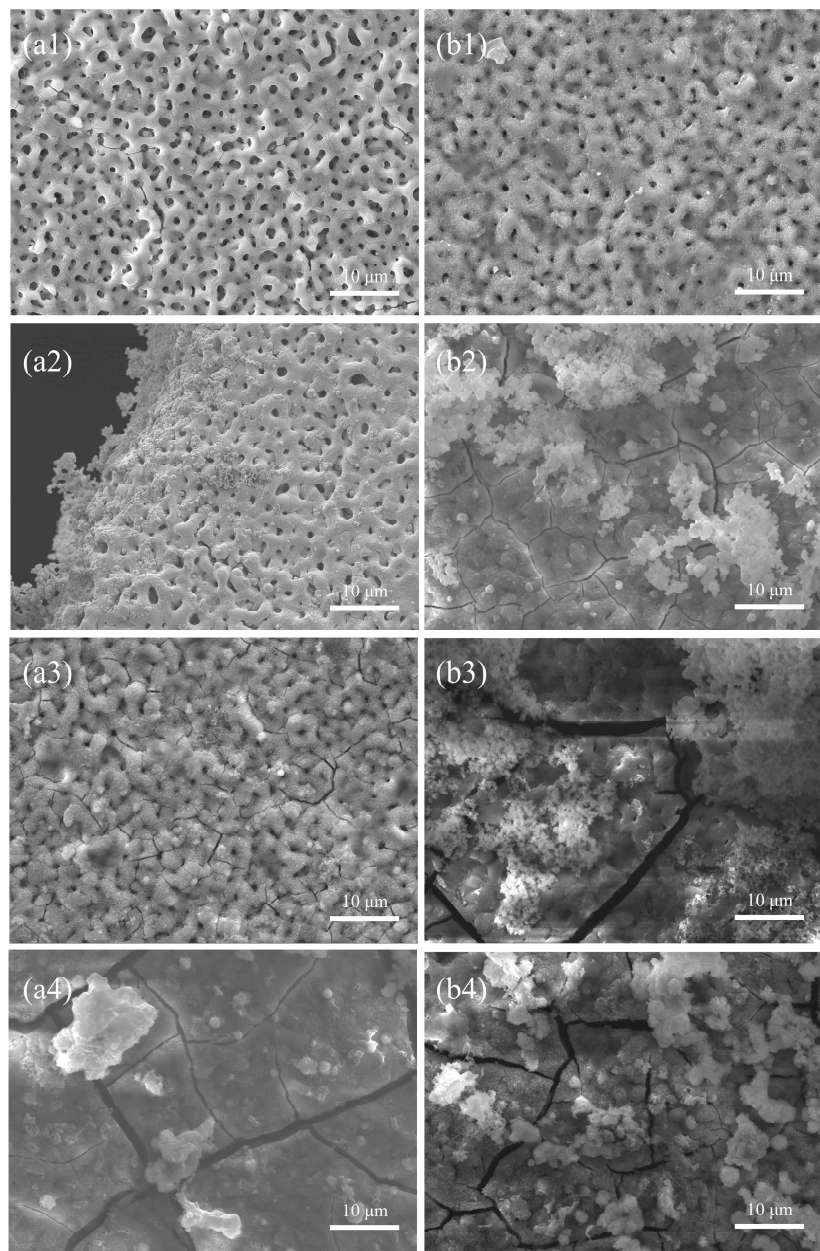


Figure 9. SEM patterns of different coatings after immersion in SBF. 0 days: (a₁) UMAO; (b₁) UMAO/PLGA/BR. 3 days: (a₂) UMAO; (b₂) UMAO/PLGA/BR. 7 days: (a₃) UMAO; (b₃) UMAO/PLGA/BR. 14 days: (a₄) UMAO; (b₄) UMAO/PLGA/BR.

3.8. Slow-Release Drug Measurements

The drug-loaded coating on the metal surface gave it functional requirements [55,56]. According to the conditions and methods under Section 2.6, the UMAO/PLGA/BR (3.0) sample was subjected to an in vitro release test. The peak area at 345 nm was measured and used to calculate the cumulative release of BR. The results are shown in Figure 10. The cumulative release of BR from the UMAO/PLGA/BR coating reached 92.13% after soaking in the SBF solution for 28 days. Peng [18] and Wang [19] studied the drugs released for 2–3 days. This prolonged the action time of the drug, increased the concentration of the drug in the local lesion, and avoided the physical and mental harm to the patient caused by long-term oral administration or external topical administration.

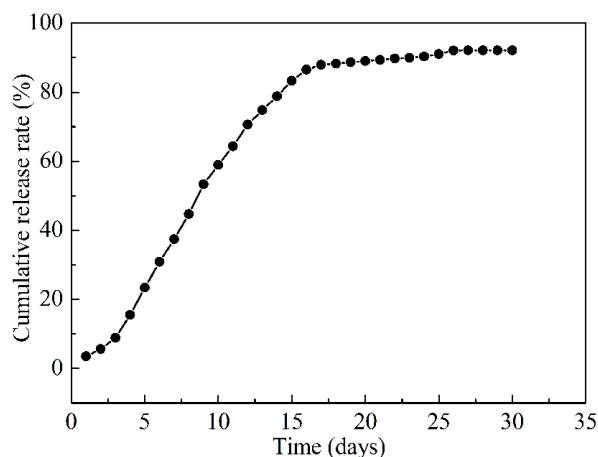


Figure 10. Cumulative release curve of the UMAO/PLGA/BR coating in vitro.

4. Conclusions

The UMAO coating has through-pores and these were sealed by the capillarity of the PLGA/BR coatings to inhibit permeation of body fluid. The corrosion resistance of the UMAO coating was significantly improved by the coverage of PLGA/BR coatings with higher impedance and lower current density. This is because the PLGA/BR coating with high cross-link density and networks has a better capacity to inhibit the permeation of ions. In addition, after the BR-loaded coating was immersed in SBF for 14 days, a large amount of substance adhered to the surface, and the prepared composite coating had excellent in vitro biological activity. After 28 days, the cumulative amount of released BR was 98.12%. Thus, the inclusion of PLGA/BR on the UMAO coatings induces an antimicrobial effect.

Author Contributions: Data analysis, L.M. and Z.M.; manuscript writing, L.M. and S.Y.; literature search, chart making, Z.M. and S.Y.; research design, J.W. and Z.M.; data collection, J.W. and L.M.; writing—original draft preparation, L.M. and S.Y.; software, L.M. and Z.M.; revise the manuscript and finalize the version to be published, L.M. and M.L. All authors have read and agreed to the published version of the manuscript.

Funding: The research was financially supported by the National Natural Science Foundation of China (No. 31370979). Fundamental Research Funds from the Provincial Education Department Fundamental Research Project, China (2019-KYYWF-1370). Jiamusi University PhD Special Scientific Research Fund Launch Project (JMSUBZ2019-10).

Conflicts of Interest: The authors declare no conflict of interest.

References

1. Raphel, J.; Holodniy, M.; Goodman, S.B.; Heilshorn, S.C. Multifunctional coatings to simultaneously promote osseointegration and prevent infection of orthopaedic implants. *Biomaterials* **2016**, *84*, 301–314. [[CrossRef](#)] [[PubMed](#)]
2. Goodman, S.B.; Yao, Z.; Keeney, M.; Yang, F. The future of biologic coatings for orthopaedic implants. *Biomaterials* **2013**, *34*, 3174–3183. [[CrossRef](#)] [[PubMed](#)]

3. Surmenev, R.A.; Surmeneva, M.A.; Ivanova, A.A. Significance of calcium phosphate coatings for the enhancement of new bone osteogenesis—A review. *Acta Biomater* **2014**, *10*, 557–579. [[CrossRef](#)] [[PubMed](#)]
4. Chen, Y.; Xu, Z.; Smith, C.; Sankar, J. Recent advances on the development of magnesium alloys for biodegradable implants. *Acta Biomater.* **2014**, *10*, 4561–4573. [[CrossRef](#)] [[PubMed](#)]
5. Li, H.; Pang, S.; Liu, Y.; Sun, L.; Liaw, P.K.; Zhang, T. Biodegradable Mg-Zn-Ca-Sr bulk metallic glasses with enhanced corrosion performance for biomedical application. *Mater. Des.* **2015**, *67*, 9–19. [[CrossRef](#)]
6. Nurettin, S.Z.; Zafer, E.V.; Said, M.K.N. Review of magnesium-based biomaterials and their applications. *J. Magnes. Alloy.* **2018**, *6*, 23–43.
7. Bakhsheshi-Rad, H.R.; Hamzah, E.; Ismail, A.F.; Aziz, M.; Daroonparvar, M.; Saebnoori, E.; Chami, A. In vitro degradation behavior, antibacterial activity and cyto-toxicity of TiO₂-MAO/ZnHA composite coating on Mg alloy for orthopedic implants. *Surf. Coat. Technol.* **2018**, *334*, 450–460. [[CrossRef](#)]
8. Razavi, M.; Fathi, M.; Savabi, O.; Vashae, D.; Tayebi, L. Regenerative influence of nanostructured bredigite (Ca₇MgSi₄O₁₆)/anodic spark coating on biodegradable AZ91 magnesium alloy implants for bone healing. *Mater. Lett.* **2015**, *155*, 97–111. [[CrossRef](#)]
9. Fierascu, I.; Fierascu, I.C.; Dinu-Pirvu, C.E.; Fierascu, R.C.; Anuta, V.; Velescu, B.S.; Jinga, M.; Jinga, V. A Short overview of recent developments on antimicrobial coatings based on phytosynthesized metal nanoparticles. *Coatings* **2019**, *9*, 787. [[CrossRef](#)]
10. Sun, J.; Zhu, Y.; Meng, L.; Chen, P.; Shi, T.; Liu, X.; Zheng, Y. Electrophoretic deposition of colloidal particles on Mg with cytocompatibility, antibacterial performance, and corrosion resistance. *Acta Biomater.* **2016**, *45*, 387–398. [[CrossRef](#)]
11. Wang, L.; Zhou, J.; Liang, J.; Chen, J. Thermal control coatings on magnesium alloys prepared by plasma electrolytic oxidation. *Appl. Surf. Sci.* **2013**, *280*, 151–155. [[CrossRef](#)]
12. Ma, C.X.; Lu, Y.; Sun, P.P.; Yuan, Y.; Jing, X.Y.; Zhang, M.L. Characterization of plasma electrolytic oxidation coatings formed on Mg-Li alloy in an alkaline polyphosphate electrolyte. *Surf. Coat. Technol.* **2011**, *206*, 287–294. [[CrossRef](#)]
13. Imwinkelried, T.; Beck, S.; Iizuka, T.; Schaller, B. Effect of a plasma electrolytic coating on the strength retention of in vivo and in vitro degraded magnesium implants. *Acta Biomater.* **2013**, *9*, 8643–8649. [[CrossRef](#)] [[PubMed](#)]
14. Cui, L.Y.; Liu, H.P.; Zhang, W.L.; Han, Z.Z.; Deng, M.X.; Zeng, R.C.; Li, S.Q.; Wang, Z.L. Corrosion resistance of a super hydrophobic micro-arc oxidation coating on mg-4li-1ca alloy. *J. Mater. Sci. Technol.* **2017**, *33*, 1263–1271. [[CrossRef](#)]
15. Zeng, R.; Zhang, F.; Song, L. Corrosion resistance of a super-hydrophobic surface on micro-arc oxidation coated mg-li-ca alloy. *J. Alloy. Compd.* **2017**, *728*, 815–826. [[CrossRef](#)]
16. Kong, K.; Hiraishi, N.; Nassar, M. Effect of phytic acidetchant on resin-dentin bonding: Monomer penetration and stability of dentin collagen. *J. Prosthodont Res.* **2016**, *61*, 251–258. [[CrossRef](#)]
17. Li, M.Q.; Liu, J.; Li, J.G. The enhanced corrosion resistance of UMAO coatings on Mg by silane treatment. *Mater. Int.* **2014**, *5*, 486–491. [[CrossRef](#)]
18. Peng, S.h.; Li, M.Q.; Wang, J.Y. Corrosion behavior and biological activity of micro-arc oxidation coating with puerarin on pure magnesium surface. *Results Phys.* **2019**, *12*, 1481–1489. [[CrossRef](#)]
19. Wang, J.Y.; Li, M.Q.; Zhang, D.Q. Corrosion resistance and cell compatibility in vitro of Chinese herbal extract coating on magnesium. *Results Phys.* **2019**, *12*, 1465–1474. [[CrossRef](#)]
20. Zhu, M.; Wang, H.; Liu, J. A mesoporous silica nanoparticu-late/β-TCP/BG composite drug delivery system for osteoarticular tuberculosis therap. *Biomaterials* **2011**, *32*, 1986–1995. [[CrossRef](#)]
21. Martínez-Vázquez, F.J.; Perera, F.H.; Miranda, P. Improving the compressive strength of bioceramic robocast scaffolds by poly-mer infiltration. *Acta Biomater.* **2010**, *6*, 4361–4368. [[CrossRef](#)] [[PubMed](#)]
22. Karacan, I.; Ben-Nissan, B.; Wang, H.A.; Juritza, A.; Swain, M.; Mueller, W.; Chu, J.; Stamboulis, A.; Macha, I.; Taraschi, V. Mechanical testing of antimicrobial biocomposite coating on metallic medical implants as drugdelivery system. *Mater. Sci. Eng. C* **2019**, *104*, 749–757. [[CrossRef](#)]
23. Colceriu, B.L.; Prejmerean, C.; Prodan, D.; Baldea, I.; Vlassa, M.; Filip, M.; Moldovan, M.; Moldovan, M.-A.; Antoniac, A.; Prejmerean, V.; et al. New pre-reacted glass containing dental composites (giomers) with improved fluoride release and biocompatibility. *Materials* **2019**, *12*, 4021. [[CrossRef](#)]

24. Borcherdig, K.; Marx, D.; Gätjen, L.; Bormann, N.; Wildemann, B.; Specht, U.; Salz, D.; Thiel, K.; Grunwald, I. Burst release of antibiotics combined with long-term release of silver targeting implant-associated infections: Design, characterization and in vitro evaluation of novel implant hybrid surface. *Materials* **2019**, *12*, 3838. [[CrossRef](#)]
25. Maydelid, T.-N.R.; Morales, A.E.; Ocampo, G. Preparation and in vitro evaluation of radiolabeled HA-PLGA nanoparticles as novel MTX delivery system for local treatment of rheumatoid arthritis. *Mater. Sci. Eng. C* **2019**, *3*, 141–152.
26. Sevostyanov, M.A.; Baikin, A.S.; Sergienko, K.V. Biodegradable stent coatings on the basis of PLGA polymers of different molecular mass, sustaining a steady release of the thrombolytic enzyme streptokinase. *React. Funct. Polym.* **2020**, *10*, 1–9. [[CrossRef](#)]
27. Qian, J.M.; Xu, W.J.; Yong, X.Q.; Jin, X.X.; Zhang, W. Fabrication and in vitro biocompatibility of biomorphic PLGA/nHA composite scaffolds for bone tissue engineering. *Mater. Sci. Eng. C* **2014**, *36*, 95–101. [[CrossRef](#)] [[PubMed](#)]
28. Wu, H.; Li, N.; Cheng, Y. In vitro Study on Biodegradable AZ31 Magnesium Alloy Fibers Reinforced PLGA Composite. *J. Mater. Sci. Technol.* **2013**, *6*, 545–550. [[CrossRef](#)]
29. Pang, W.Y.; Wang, X.L.; Mok, S.K.; Lai, W.P.; Chow, H.K.; Leung, P.C.; Yao, X.S.; Wong, W.S. Naringin improves bone properties in ovariectomized mice and exerts oestrogenlike activities in rat osteoblast-like (UMR106) cells. *Br. J. Pharmacol.* **2010**, *159*, 1693–1703. [[CrossRef](#)]
30. Wu, J.-B.; Fong, Y.-C.; Tsai, H.-Y.; Chen, Y.-F.; Tsuzuki, M.; Tang, C. Naringin-induced bone morphogenetic protein-2 expression via PI3K, Akt, c-Fos/c-Jun and AP-1 pathway in osteoblasts. *Eur. J. Pharmacol.* **2008**, *588*, 333–341. [[CrossRef](#)]
31. Afewerki, S.; Bassous, N.; Harb, S.; Palo-Nieto, C.; Ruiz-Esparza, G.U.; Marciano, F.R.; Webster, T.J.; Furtado, A.S.A.; Lobo, A.O. Advances in dual functional antimicrobial and osteoinductive biomaterials for orthopaedic applications. *Nanomed. Nanotechnol. Biol. Med.* **2020**, *24*, 102–113. [[CrossRef](#)] [[PubMed](#)]
32. Waterman, J.; Pietak, A.; Birbilis, N.; Woodfield, T.; Dias, G.; Staiger, M.P. Corrosion resistance of biomimetic calcium phosphate coatings on magnesium due to varying pretreatment time. *Mater. Sci. Eng. B* **2011**, *20*, 1756–1760. [[CrossRef](#)]
33. Cui, L.Y.; Gao, S.D.; Li, P.P.; Zeng, R.C.; Zhang, F.; Li, S.Q. Corrosion resistance of a self-healing micro-arc oxidation/poly methyltrimethoxysilane composite coating on magnesium alloy az31. *Corros. Sci.* **2017**, *118*, 84–95. [[CrossRef](#)]
34. Wang, Y.M.; Guo, J.W.; Wu, Y.F. Biocorrosion resistance of coated magnesium alloy by microarc oxidation in electrolyte containing zirconium and calcium salts. *Front. Mater. Sci.* **2014**, *20*, 256–366. [[CrossRef](#)]
35. Li, J.N.; Cao, P.; Zhang, X.N.; Zhang, S.X.; He, Y.H. In vitro degradation and cell attachment of a PLGA coated biodegradable Mg–6Zn based alloy. *J. Mater. Sci.* **2010**, *45*, 6038–6045. [[CrossRef](#)]
36. Batra, U.; Kapoor, S.; Sharma, S. Influence of Magnesium Ion Substitution on Structural and Thermal Behavior of Nanodimensional Hydroxyapatite. *J. Mater. Eng. Perform.* **2013**, *22*, 1798–1806. [[CrossRef](#)]
37. Diana, M.V.; Ionut, C.I.; Elena, U. Magnesium Doped Hydroxyapatite-Based Coatings Obtained by Pulsed Galvanostatic Electrochemical Deposition with Adjustable Electrochemical Behavior. *Coatings* **2020**, *10*, 2–17.
38. Zhang, F.; Zhang, C.; Song, L.; Zeng, R.-C.; Li, S.; Cui, H. Fabrication of the Superhydrophobic Surface on Magnesium Alloy and Its Corrosion Resistance. *J. Mater. Sci. Technol.* **2015**, *31*, 1139–1143. [[CrossRef](#)]
39. Taheri, M.; Kish, J.; Birbilis, N.; Danaie, M.; McNally, E.; McDermid, J. Towards a Physical Description for the Origin of Enhanced Catalytic Activity of Corroding Magnesium Surfaces. *Electrochim. Acta* **2014**, *116*, 396–403. [[CrossRef](#)]
40. Mousa, H.M.; Lee, D.H.; Kim, C.S.; Kim, C.S. A novel simple strategy for in situ deposition of apatite layer on AZ31B magnesium alloy for bone tissue regeneration. *Appl. Surf. Sci.* **2015**, *351*, 55–65. [[CrossRef](#)]
41. Vaz, J.M.; Taketa, T.B.; Hernandez-Montelongo, J.; Chevallier, P.; Cotta, M.A.; Mantovani, D.; Beppu, M.M. Antibacterial properties of chitosan-based coatings are affected by spacer-length and molecular weight. *Appl. Surf. Sci.* **2018**, *445*, 478–487. [[CrossRef](#)]
42. Pozzo, L.D.Y.; Conceição, T.; Spinelli, A.; Scharnagl, N.; Pires, A.T. Chitosan coatings crosslinked with genipin for corrosion protection of AZ31 magnesium alloy sheets. *Carbohydr. Polym.* **2018**, *181*, 71–77. [[CrossRef](#)] [[PubMed](#)]
43. Toorani, M.; Aliofkhaei, M. Review of electrochemical properties of hybrid coating systems on Mg with plasma electrolytic oxidation process as pretreatment. *Surf. Interfaces* **2019**, *14*, 262–295. [[CrossRef](#)]

44. Zhang, X.P.; Zhao, Z.P.; Wu, F.M.; Wang, Y.L.; Wu, J. Corrosion and wear resistance of AZ91D magnesium alloy with and without microarc oxidation coating in Hank's solution. *J. Mater. Sci.* **2007**, *42*, 8523–8528. [[CrossRef](#)]
45. Razavi, M.; Fathi, M.; Savabi, O.; Beni, B.H.; Vashae, D.; Tayebi, L. Surface microstructure and in vitro analysis of nanostructured akermanite ($\text{Ca}_2\text{MgSi}_2\text{O}_7$) coating on biodegradable magnesium alloy for biomedical applications. *Colloids Surfaces B: Biointerfaces* **2014**, *117*, 432–440. [[CrossRef](#)]
46. Chen, J.; Wang, J.; Han, E.; Dong, J.; Ke, W. AC impedance spectroscopy study of the corrosion behavior of an AZ91 magnesium alloy in 0.1M sodium sulfate solution. *Electrochim. Acta* **2007**, *52*, 3299–3309. [[CrossRef](#)]
47. Liu, M.; Schmutz, P.; Uggowitzer, P.J.; Song, G.-L.; Atrens, A. The influence of yttrium (Y) on the corrosion of Mg–Y binary alloys. *Corros. Sci.* **2010**, *52*, 3687–3701. [[CrossRef](#)]
48. Niu, B.; Shi, P.; Shanshan, E.; Wei, D.; Li, Q.; Chen, Y. Preparation and characterization of HA sol–gel coating on MAO coated AZ31 alloy. *Surf. Coat. Technol.* **2016**, *286*, 42–48. [[CrossRef](#)]
49. Zhang, M.; Cai, S.; Zhang, F.; Xu, G.; Wang, F.; Yu, N.; Wu, X. Preparation and corrosion resistance of magnesium phytic acid/hydroxyapatite composite coatings on biodegradable AZ31 magnesium alloy. *J. Mater. Sci. Mater. Electron.* **2017**, *28*, 82. [[CrossRef](#)]
50. Jamesh, M.; Kumar, S.; Sankara, N.T. Electrode position of Hydroxyapatite Coating on Magnesium for Biomedical Applications. *J. Coat. Technol. Res.* **2011**, *4*, 495–502.
51. Bhattacharjee, A.; Gupta, A.; Verma, M.; Anand, M.P.; Sengupta, P.; Saravanan, M.; Manna, I.; Balani, K. Antibacterial and magnetic response of site-specific cobalt incorporated hydroxyapatite. *Ceram. Int.* **2020**, *46*, 513–522. [[CrossRef](#)]
52. Wang, H.; Eliaz, N.; Xiang, Z.; Hsu, H.P.; Spector, M.; Hobbs, L.W. Early bone apposition in vivo on plasma-sprayed and electrochemically deposited hydroxyapatite coatings on titanium alloy. *Biomaterials* **2006**, *27*, 4192–4203. [[CrossRef](#)] [[PubMed](#)]
53. Cheon, K.H.; Gao, C.; Kang, M.H.; Jung, H.D.; Jang, T.S.; Kim, H.E. A crack-free anti-corrosive coating strategy for magnesium implants under deformation. *Corros. Sci.* **2017**, *11*, 6–24. [[CrossRef](#)]
54. Müller, L.; Müller, F.A. Preparation of SBF with different HCO_3^- content and its influence on the composition of biomimetic apatites. *Acta Biomater.* **2006**, *2*, 181–189. [[CrossRef](#)] [[PubMed](#)]
55. Maczynska, B.; Secewicz, A.; Smutnicka, D.; Szymczyk, P.; Dudek-Wicher, R.; Junka, A.; Bartoszewicz, M. In vitro efficacy of gentamicin released from collagen sponge in eradication of bacterial biofilm preformed on hydroxyapatite surface. *PLoS ONE* **2019**, *14*, 217–229. [[CrossRef](#)]
56. Llorens, E.; Calderon, S.; Del Valle, L.J.; Puiggali, J. Polybiguanide (PHMB) loaded in PLA scaffolds displaying high hydrophobic, biocompatibility and antibacterial properties. *Mater. Sci. Eng. C* **2015**, *50*, 74–84. [[CrossRef](#)]

